

## PAPER

[View Article Online](#)  
[View Journal](#) | [View Issue](#)Cite this: *J. Mater. Chem. A*, 2019, 7, 25165

## Strategic hierarchical improvement of superprotonic conductivity in a stable metal–organic framework system†

Xiao-Min Li,<sup>a</sup> Jiang Liu,<sup>\*a</sup> Chen Zhao,<sup>a</sup> Jia-Lin Zhou,<sup>a</sup> Ling Zhao,<sup>ID \*b</sup> Shun-Li Li<sup>a</sup> and Ya-Qian Lan<sup>ID \*a</sup>

Identification of proton-exchange membranes (PEMs) with high proton conductivity and long-term durability is highly important for the development of fuel cells. Herein, an efficient and feasible strategy that features different proton sources and hopping site modifications on the stable UiO-66-NH<sub>2</sub> framework for hierarchically improving the proton conductivity is demonstrated. As a result, IM-UiO-66-AS showed the highest superprotonic conductivity of  $1.54 \times 10^{-1} \text{ S cm}^{-1}$  (80 °C, 98% RH) and outstanding long-term durability of at least 100 h, which surpass those of all the reported proton-conducting MOF materials without guest loading. Furthermore, the manufactured membrane could maintain a high proton conductivity of  $1.19 \times 10^{-2} \text{ S cm}^{-1}$  even with continuous work for at least 40 h under the same conditions, suggesting its great potential for further application in devices.

Received 18th September 2019  
Accepted 10th October 2019

DOI: 10.1039/c9ta10286h

[rsc.li/materials-a](http://rsc.li/materials-a)

## Introduction

Proton exchange membrane fuel cells (PEMFCs) are considered to be promising devices in the development of clean and renewable energy due to their high energy density, environmental friendliness and gentle operating environment.<sup>1</sup> Proton exchange membrane (PEM) is the core component of PEMFCs that separates the fuel from the oxidant and allows protons to pass freely through the membrane,<sup>2,3</sup> which are fundamental to the life and performance of the battery. The requirements for PEMs in actual applications are as follows: (i) high proton conductivity ( $>10^{-2} \text{ S cm}^{-1}$ ) to promote efficient proton transfer between the electrodes;<sup>4</sup> (ii) good thermal and chemical stability to guarantee the performance of the electrolyte in the operating state of the fuel cell;<sup>5,6</sup> (iii) being fabricated into a membrane;<sup>7</sup> (iv) low cost and (v) easy processing.<sup>8</sup> Currently, the commercially available proton exchange membrane is Nafion,<sup>9,10</sup> which has high proton conductivity but is costly.<sup>11</sup> Therefore, constructing inexpensive and stable materials with high proton conductivity is the research direction for the next generation of PEM materials.

The ionic conductivity formula of  $\sigma = zen\mu$  ( $n$ ,  $z$ ,  $e$  and  $\mu$  denote the valence of ion, elemental charge, charge carrier concentration and carrier mobility respectively)<sup>12</sup> indicates that

increasing the number of proton hopping sites and proton sources is necessary for efficient proton transmission<sup>13</sup> and realizing high proton conductivity in a material, because the charge carrier concentration and mobility positively correlate with the proton source and hopping frequency, respectively.<sup>14</sup> Therefore, the higher these two factors are, the better will be the theoretical performance. In recent years, metal organic framework (MOF) materials with proton conductivity have been developed rapidly.<sup>15–23</sup> The main advantages of these MOF-based proton conductors are as follows: firstly, their crystalline nature can provide a visualization platform for the investigation of the proton transfer mechanism.<sup>24,25</sup> Secondly, their pores/channels can furnish a pathway for proton transfer.<sup>26,27</sup> Thirdly, the number of proton hopping sites and proton sources can be increased by means of specific modifications or post-synthesis steps on the functionalized organic linkers, which then endow the material with high proton conductive performance.<sup>28–31</sup> So far, the highest performance among the reported proton conductive MOF materials has reached up to  $10^{-2} \text{ S cm}^{-1}$ , and not all the materials have been fabricated further into membranes for devices.<sup>32–35</sup> The reason for this fact may be that their performances were inadequate for device applications. Furthermore, the structures of most MOFs are unstable and liable to collapse under high temperature and high humidity conditions,<sup>36,37</sup> which severely limit their application in devices. Therefore, strategically improving the proton conductivity and maintaining the structural stability of the material are extremely important foundations for further its device application as a PEM.

Based on the above considerations, we expected to improve proton conductivity in a stable MOF structural model system by

<sup>a</sup>School of Chemistry and Materials Science, Nanjing Normal University, Nanjing 210023, P. R. China. E-mail: liuj@njnu.edu.cn; yqlan@njnu.edu.cn<sup>b</sup>Department of Material Science and Chemistry, China University of Geosciences, Wuhan 430074, China. E-mail: zhaoling@cug.edu.cn

† Electronic supplementary information (ESI) available: Experimental methods and supporting figures and tables. See DOI: 10.1039/c9ta10286h

increasing the proton hopping sites and proton sources step by step and then achieve device-oriented conditions. UiO-66 has well-known highly structural and chemical stabilities,<sup>38</sup> and its terephthalic acid ligands can be modified by amino groups (can serve as proton hopping sites)<sup>39</sup> and sulfonic acid groups (can serve as proton hopping sites and proton sources<sup>40</sup>). Consequently, we chose this MOF model to achieve the above strategy to enhance proton conductivity. Initially, we synthesized **UiO-66-NH<sub>2</sub>** (zero proton source and one hopping site) (Scheme 1a) as the starting material, followed by the partial substitution of the ligand 2-aminoterephthalic acid (BDC-NH<sub>2</sub>) with monosodium 2-sulfoterephthalate (BDC-SO<sub>3</sub>Na) to get **UiO-66-AS** (AS represents the amino and sulfonic acid groups, respectively) (one proton source and two hopping sites). It is well-known that protons generated by the acidic groups on the organic linkers of the framework are steadier than those of the acidic molecules encapsulated in the pores.<sup>41</sup> Additionally, introducing sulfonic acid groups, which have a low  $pK_a$ , is the perfect approach for improving the proton conductivity because they can stoichiometrically form  $H_3O^+$  ions (regarded as proton carriers) with  $H_2O$  molecules.<sup>12</sup> Afterwards, the residual uncoordinated amino groups were covalently connected to the aldehyde groups of imidazole-2-carboxaldehyde by a Schiff base reaction<sup>42</sup> to form **IM-UiO-66-AS** (two proton sources and four hopping sites) (Scheme 1b).

We have successfully implemented the above tactic and eventually achieved extremely high proton conductivity in **IM-UiO-66-AS**. It exhibited a superprotonic conductivity of  $1.54 \times 10^{-1} \text{ S cm}^{-1}$  at 80 °C and 98% relative humidity (RH), which is the highest for a stand-alone proton-conducting MOF material without guest loading, and also showed outstanding long-term stability with a negligible loss after continuously working for 100 hours. In particular, based on its high proton conductivity and structural stability, this compound was further fabricated into a membrane (abbreviated as **IM-UiO-66-AS@PP** membrane), which maintained a high proton conductivity of  $1.19 \times 10^{-2} \text{ S cm}^{-1}$  (80 °C, 98% RH) along with a durability of at least 40 h.

## Results and discussion

### Characterization of the materials (powder)

Microcrystals of **UiO-66-NH<sub>2</sub>** were synthesized according to a previously described method in the literature. The powder X-ray diffraction (PXRD) patterns demonstrated that the structures of **UiO-66-AS** and **IM-UiO-66-AS** retained the host

framework of **UiO-66-NH<sub>2</sub>** and their pore spaces, which could be inferred from the sharp reflections at lower angles<sup>43</sup> (Fig. 1a). The control samples **UiO-66-SO<sub>3</sub>H** and **UiO-66-NH<sub>2</sub>-IM** matched well with the simulated pattern, proving that they had a similar framework structure as the host compound (Fig. S1†). In addition, the PXRD patterns in Fig. S2† demonstrate that **IM-UiO-66-AS** soaked in sulfuric acid solutions (pH = 1, 3 and 5) maintained the structural robustness. Furthermore, the scanning electron microscopy (SEM) images of **UiO-66-NH<sub>2</sub>**, **UiO-66-AS** and **IM-UiO-66-AS** displayed analogous morphological features and grain sizes (Fig. 1c, S3 and S4†). Meanwhile, the **IM-UiO-66-AS** particles observed by transmission electron microscopy (TEM) exhibited unchanged morphology, and the selected area electron diffraction pattern of the powder is shown in Fig. 1d. Proof for the successful substitution of BDC-NH<sub>2</sub> with BDC-SO<sub>3</sub>H and the completion of reaction between **UiO-66-AS** and imidazole-2-carboxaldehyde were confirmed *via* the FT-IR spectra of **UiO-66-NH<sub>2</sub>**, **UiO-66-AS** and **IM-UiO-66-AS**. The clues in Fig. 1b evidently revealed that the vibrational bands of -NH<sub>2</sub> groups in **UiO-66-NH<sub>2</sub>** and **UiO-66-AS** emerged in the range of 3300–3500  $\text{cm}^{-1}$ . Besides, the relatively strong band located seen at 1656  $\text{cm}^{-1}$  can be ascribed to the bending vibration of the -NH<sub>2</sub> group, illustrating the presence of -NH<sub>2</sub> groups in **UiO-66-NH<sub>2</sub>** and **UiO-66-AS**.<sup>44,45</sup> The -SO<sub>3</sub>H groups appeared after the first modification, which was deduced from the characteristic peak of 625  $\text{cm}^{-1}$ . Moreover, the bands at 1065  $\text{cm}^{-1}$  and 1025  $\text{cm}^{-1}$  appearing in the FT-IR spectra of **UiO-66-AS** and **IM-UiO-66-AS** belonged to the S=O groups, indicating the success of the first modification.<sup>46</sup> The reflectance FT-IR spectrum of **IM-UiO-66-AS** exhibited a new band at 1654  $\text{cm}^{-1}$ , corresponding to the vibrational band of the emerging imine group from the condensation reaction of

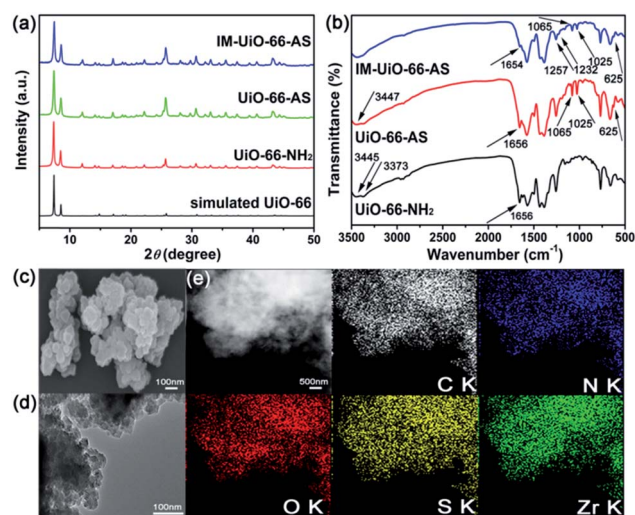
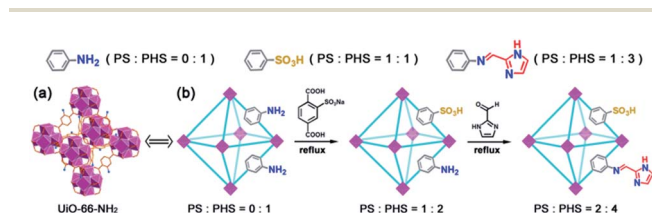


Fig. 1 (a) PXRD patterns of simulated UiO-66 (black), as-synthesized UiO-66-NH<sub>2</sub> (red), as-synthesized UiO-66-AS (green) and as-synthesized IM-UiO-66-AS (blue). (b) FT-IR spectra of as-synthesized UiO-66-NH<sub>2</sub> (black), as-synthesized UiO-66-AS (red) and as-synthesized IM-UiO-66-AS (blue). (c) SEM image of as-synthesized IM-UiO-66-AS. (d) TEM image of as-synthesized IM-UiO-66-AS. (e) Element mapping images of IM-UiO-66-AS (C, N, O, S and Zr).



Scheme 1 (a) Structure of **UiO-66-NH<sub>2</sub>**. (b) Schematic illustration of the preparation of the **IM-UiO-66-AS** composite material. PS: proton source and PHS: proton hopping site.

aldehyde and amine.<sup>47</sup> The band at  $1232\text{ cm}^{-1}$  appeared after the covalent modification, owing to the C–N stretching vibrations of imidazole-2-carboxaldehyde.<sup>45</sup> Additionally, an observable decrease of the relative intensity of the C–N stretching vibration band of 2-aminoterephthalic acid ( $\sim 1257\text{ cm}^{-1}$ ) occurred owing to the appearance of the new imine (C=N) groups, representing the successful transformation from amino groups to imine groups.<sup>48</sup> Furthermore, the  $^{13}\text{C}$  CP/MAS NMR spectra were recorded to further demonstrate the successful synthesis of **IM-UiO-66-AS**. In Fig. S5,† the typical signal of carbon from the C=N group can be observed at 165.28 ppm, testifying the generation of a new imine group. In the meantime, as shown in Fig. S6, S7 and Table S1,† the decreased  $\text{N}_2$  adsorption data indirectly implied that the sulfonated ligands partially substituted the amino-based ligands. At the same time, the decreased pore volume indicated that imidazole-2-carboxaldehyde covalently reacted with an amino group occupying a certain pore space of the host framework. Thermogravimetric analysis showed differences between before and after modification, indicating new species formation (Fig. S8–S10†). Element mapping images of **IM-UiO-66-AS** also showed that the elements C, N, O, S and Zr were homogeneously distributed (Fig. 1e). Furthermore, the energy dispersive X-ray (EDX) results shown in Fig. S11–S13† clearly confirmed the presence of S element in **UiO-66-AS** and **IM-UiO-66-AS** compared to the original material **UiO-66-NH<sub>2</sub>**. To further verify the result of EDX, we conducted elemental analysis to observe the changes in the content of element N, which experiences the process of decrease and increase due to the replacement of amino groups first and then the introduction of imidazole groups, respectively, along with the appearance of element S due to the introduction of sulfonic acids (Table S2†). Simultaneously, in order to obtain more accurate elemental content data, we also carried out inductively coupled plasma mass measurement, which showed the same mass percentages (Table S3†). According to the above results, the fact that 20% of the amino-based terephthalic acid ligands were replaced by sulfonated ligands during the substitution process is evident, and the content of element S remained unchanged in **IM-UiO-66-AS** compared to that in **UiO-66-AS**. As for the content of element N, it shows that almost all the amino-based ligands in the activated sample participated in the Schiff base reaction.

### Proton conduction of the materials (powder)

In order to verify the effect of the **UiO-66-NH<sub>2</sub>** modification strategy of increasing the proton sources and hopping sites to improve the proton conductivity, we used alternating current (AC) impedance spectroscopy to study the proton conductivities of the different as-synthesized compounds in the shape of compressed pellets at a constant temperature of  $30\text{ }^\circ\text{C}$  and under a humidity range of 40–98% RH. As shown in Fig. S14–S18,† it was obvious that the conductivity of all the synthetic samples presented notable positive correlations with the varying humidity, implying that water molecules had a direct impact on proton conduction owing to its ability to form an efficient hydrogen bonding network in the conjugate acid-base

system ( $\text{H}_3\text{O}^+ + \text{H}_2\text{O} \leftrightarrow \text{H}_2\text{O} + \text{H}_3\text{O}^+$ ). In the water uptake curves, **UiO-66-SO<sub>3</sub>H** showed the largest water adsorption capacity, and **IM-UiO-66-AS** was the second (Fig. S19a†). Furthermore, as shown in Fig. S19b,† the desorption isotherm of **IM-UiO-66-AS** exhibited hysteresis, which may be caused by capillary action. Moreover, all materials retain their structural integrity after undergoing water adsorption measurements (Fig. S20†). Additionally, the signal of carbon from the C=N group could be observed at 162.46 ppm, which shows that **IM-UiO-66-AS** was not hydrolyzed and maintained its structure after the water adsorption measurement (Fig. S21†). Thus, the pellets could retain more water by the auxiliary effect of the hydrophilic groups and ultimately reduce the grain boundaries between particles as much as possible.<sup>41</sup> The Nyquist plots of all composites at a fixed temperature ( $30\text{ }^\circ\text{C}$ ) and different humidity conditions (40–98% RH) are shown in Fig. S22–S26,† in which the semicircle of the high frequency region relates to the bulk and grain boundary resistances, and the tail portion of the low frequency region corresponds to the moving ions clogged by the interface between the electrode and electrolyte.<sup>49,50</sup> Besides, two clear semicircles appeared in the high frequency region of some impedance plots, from which we chose the higher-frequency one for fitting and computing the bulk resistance.<sup>32</sup> In order to verify whether the sulfonic acid ligands in the **UiO-66-AS** pores were cleaned up, we also tested the proton conductivity of **UiO-66-AS** without cleaning the channels (Fig. S27†) and obtained the value of  $5.81 \times 10^{-3}\text{ S cm}^{-1}$  at  $30\text{ }^\circ\text{C}$  and 98% RH, which is 37 times more than that of activated **UiO-66-AS** ( $1.55 \times 10^{-4}\text{ S cm}^{-1}$ ). The obvious difference indicated that most of the free guest molecules in the MOF channels had been washed away by the activation procedures, further confirming that guests in the MOF channels can be largely removed. Moreover, all the materials showed much lower proton conductivities at 40% RH, indicating that  $\text{H}_2\text{O}$  molecules play a significant role in proton transport (Fig. S28–S32†).

Another important factor that can affect proton conduction is temperature, which is also positively associated with the value of proton conductivity. The Nyquist plot of **IM-UiO-66-AS** at  $80\text{ }^\circ\text{C}$  shown in Fig. 2a also presents an arc and a tail in the high and low frequency regions, respectively. Meanwhile, ZView software was used to fit the impedance values to get an equivalent circuit at  $80\text{ }^\circ\text{C}$  and 98% RH (Fig. S33†), and the relative parameters are shown in Table S4.† The conductivity of **IM-UiO-66-AS** monotonically increased with increasing temperature (Fig. 2b), and the great advantage of **IM-UiO-66-AS** was also evident from its proton conductivity. As shown in Fig. 2b, **UiO-66-AS** displayed performance of  $1.7 \times 10^{-4}\text{ S cm}^{-1}$  ( $80\text{ }^\circ\text{C}$ ) due to the addition of one proton source and one hopping site. The supplementary hydrophilic sulfonic acid groups are recognized as proton sources as they can assist in absorbing more water molecules under high relative humidity to elevate the proton conductivity. Because of one added proton source and two added hopping sites, **IM-UiO-66-AS** achieved a maximal value of  $1.54 \times 10^{-1}\text{ S cm}^{-1}$  ( $80\text{ }^\circ\text{C}$ ) after the second modification, which is almost 5 orders of magnitude higher than that of pristine **UiO-66-NH<sub>2</sub>**. Thus, it is the highest proton conducting MOF material that transmits protons mainly using its functionalized



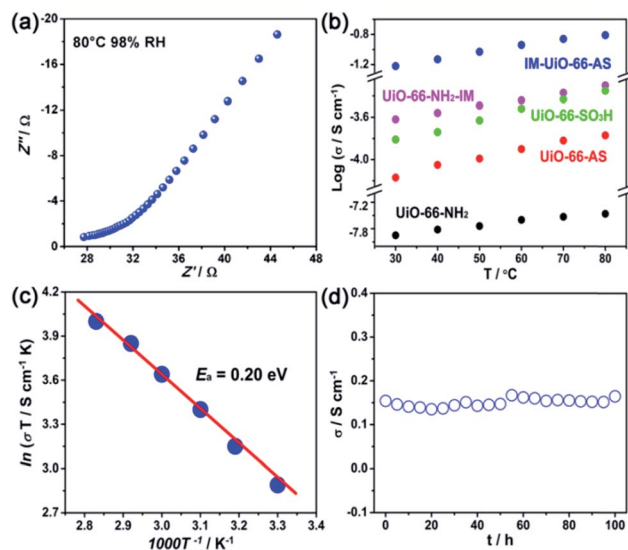


Fig. 2 (a) The Nyquist plot of IM-UiO-66-AS at 80 °C and under 98% RH. (b) Temperature-dependent proton conductivities of UiO-66-NH<sub>2</sub> (black), UiO-66-AS (red), UiO-66-SO<sub>3</sub>H (green), UiO-66-NH<sub>2</sub>-IM (magenta) and IM-UiO-66-AS (blue) (98% RH, 30–80 °C). (c) Arrhenius plot of IM-UiO-66-AS under 98% RH in the temperature range of 30–80 °C. (d) Time-dependent proton conductivity of IM-UiO-66-AS performed at 80 °C and under 98% RH.



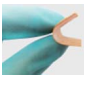
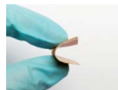
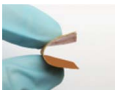
groups rather than guest loading (Table S5<sup>†</sup>). Besides, it is undeniable that after the activation treatment, the residual guest molecules in the MOF channels can also make a small contribution to proton conduction. Furthermore, UiO-66-SO<sub>3</sub>H and UiO-66-NH<sub>2</sub>-IM respectively exhibited the proton conducting performances of  $4.46 \times 10^{-4} \text{ S cm}^{-1}$  and  $5 \times 10^{-4} \text{ S cm}^{-1}$  at 80 °C, both of which are inferior to that of IM-UiO-66-AS. In addition, all the Nyquist plots shown in Fig. S34<sup>†</sup> intuitively suggested that IM-UiO-66-AS had the lowest resistance among all the tested compounds. The meaning of activation energy allows an in-depth understanding of the proton conduction mechanism, and hence, we fitted and calculated the activation energy ( $E_a$ ) at 98% RH. As shown in Fig. 2c, the value of  $E_a$  of IM-UiO-66-AS was 0.20 eV, which can be classified as the Grotthuss mechanism. Except for the  $E_a$  of UiO-66-NH<sub>2</sub> in Fig. S35<sup>†</sup> corresponding with vehicle mechanism, the values of  $E_a$  of UiO-66-AS, UiO-66-SO<sub>3</sub>H and UiO-66-NH<sub>2</sub>-IM are also within the scope of <0.40 eV, which belong to the Grotthuss mechanism (Fig. S36–S38<sup>†</sup>). Further, excellent performance durability is integral to proton conduction-based applications. Accordingly,

time-dependent measurement of IM-UiO-66-AS was executed at 80 °C and 98% RH. As shown in Fig. 2d, it was found that IM-UiO-66-AS retained high proton conductivity even after 100 hours, and the loss of conductivity was negligible. Therefore, it can currently be considered the most stable proton conductor based on a MOF with high proton conductivity. In order to shed light on whether the high conductivity of IM-UiO-66-AS can withstand a wider temperature range, temperature-dependent conductivity measurement was carried out under heating and cooling cycles ranging from 30–80 °C under 98% RH (Fig. S39<sup>†</sup>). It could be grasped from Fig. S40<sup>†</sup> that the conductivity values in the heating periods of IM-UiO-66-AS basically coincided with those in the cooling periods for the same temperatures, which is a very valuable reference factor for further reuse of fuel cells. The little deviation in conductivity value may be due to insufficient reabsorption of water molecules by the sample during the cooling period.<sup>51</sup> Remarkably, the corresponding PXRD patterns of all the materials after proton conduction measurements were identical to that of the parent material (Fig. S41<sup>†</sup>), proving that the materials had excellent stability, which is essential for their practical application in fuel cells. In addition, the signal of carbon from the C=N group at 162.72 ppm in the solid state <sup>13</sup>C CP/MAS NMR spectrum of IM-UiO-66-AS testified that there was no hydrolysis of the imine group during proton conduction measurement (Fig. S42<sup>†</sup>).

### Characterization and proton conduction of the materials (membrane)

To study the potential of IM-UiO-66-AS in devices, we used the microcrystalline powder of IM-UiO-66-AS as a filler and dispersed it in a PVDF-PVP composite carrier to prepare a hybrid matrix membrane with good stability and high proton conductivity, as an important step towards practical applications. Similarly, we also fabricated membranes with all the control samples to study their proton conducting performances to embody the superiority of the IM-UiO-66-AS@PP membrane. It can be seen from Table 1 and Fig. S43<sup>†</sup> that we synthesized hybrid membranes from all the materials and their structures maintained the framework of UiO-66. The morphology and thickness of all the membranes are presented in Fig. S44–S48<sup>†</sup>. As shown in Fig. S49–S53<sup>†</sup>, the hybrid membranes had good thermal stability. Moreover, the mechanical property of the IM-UiO-66-AS@PP membrane was evaluated (Fig. S54<sup>†</sup>), and the relevant results are listed in Table S6<sup>†</sup> from which we can see that the elastic modulus was 152.98 MPa, and the ultimate

Table 1 Conductivity ( $\sigma$ ) values at 80 °C and 98% RH and images of the membranes

Compound	UiO-66-NH <sub>2</sub>	UiO-66-SO <sub>3</sub> H	UiO-66-AS	UiO-66-NH <sub>2</sub> -IM	IM-UiO-66-AS
$\sigma$ (S cm <sup>-1</sup> ) (powder)	$3 \times 10^{-6}$	$4.46 \times 10^{-4}$	$1.7 \times 10^{-4}$	$5 \times 10^{-4}$	$1.54 \times 10^{-1}$
Image (membrane)					
$\sigma$ (S cm <sup>-1</sup> ) (membrane)	$9.11 \times 10^{-7}$	$1.17 \times 10^{-4}$	$1.91 \times 10^{-5}$	$1.59 \times 10^{-4}$	$1.19 \times 10^{-2}$

tensile strength was 4.62 MPa. With the further aim of exploring the proton conductivities of membranes under varying humidity, we executed tests to obtain Nyquist plots from AC impedance data at a fixed temperature (30 °C) and different humidity conditions (40–98% RH) (Fig. S55–S59†) and discovered a significantly positive relationship between proton conductivity and relative humidity (Fig. S60–S64†), signifying that water molecules were firmly the driving force of proton conduction. Under high humidity conditions, loose water molecules on the surface of the composite membrane are free to permeate and fill the membrane material, which can largely eliminate the grain boundary resistance of the material and ameliorate the proton conductivity.

To determine the effect of temperature on the proton conductivity of the membranes, we conducted the temperature dependent conductivity measurements at 98% RH. The Nyquist diagram of the IM-UiO-66-AS@PP membrane presented in Fig. 3a at 80 °C and 98% RH could be fitted to obtain a conductivity of  $1.19 \times 10^{-2} \text{ S cm}^{-1}$ . Similarly, the equivalent circuit is displayed in Fig. S65,† and the fitted parameters are shown in Table S7.† The specific conductivity values rise with the increase in temperature in Fig. 3b, along with the more important conclusion that the IM-UiO-66-AS@PP membrane had the highest value of proton conductivity. Our in-depth knowledge of the proton transport mechanism originates from the activation energy ( $E_a$ ) derived from the Arrhenius plots. As shown in Fig. 3c, the value of  $E_a$  of the IM-UiO-66-AS@PP membrane was 0.32 eV, which can be classified as the Grotthuss mechanism. At the same time, the  $E_a$  of the other complex membranes displayed in Fig. S66–S69† reveal that the Grotthuss

mechanism for proton transport occurs in hybrid membranes. Likewise, in order to ascertain the temperature dependence of the conductivity of the target membrane, proton conductivity determination was performed at 98% RH with heating from 30–80 °C and cooling from 80–30 °C (Fig. S70†). The result in Fig. S71† states clearly that the conductivity of the IM-UiO-66-AS@PP membrane is, in general, in accordance with the temperature. Besides, the IM-UiO-66-AS@PP membrane also exhibited good retention of performance, as shown in Fig. 3d, with almost no loss after 40 hours, which is an important foundation and guarantee for implementation. What makes sense is that the structures remained intact after the test (Fig. S72†). We also tried to increase the content of **IM-UiO-66-AS** in the fabricated composite membrane, but the conductivity performance did not further improve (Fig. S73–S74†). The proton conductivities were  $1.13 \times 10^{-2} \text{ S cm}^{-1}$  for 80 wt% MOF and  $1.32 \times 10^{-2} \text{ S cm}^{-1}$  for 100 wt% MOF, both of which are within a reasonable error range, compared to the conductivity value of  $1.19 \times 10^{-2} \text{ S cm}^{-1}$  for 60 wt% MOF (80 °C, 98% RH). As seen from Table S8†, only a few works concerning proton conducting MOF membranes have been published, and reports on the dependence of proton transfer on the MOF itself rather than the polymer matrix are even fewer. All the above conclusions suggest that the IM-UiO-66-AS@PP membrane is likely to have great potential for applications.

### Fuel cell performance

Furthermore, to explore the practical applications of the membrane as the electrolyte, we assembled an  $\text{H}_2/\text{O}_2$  fuel cell with the IM-UiO-66-AS@PP membrane. As shown in Fig. S75,† the maximum open-circuit voltage was 0.78 V at 80 °C and 98% RH, which is similar to other reported PEMFCs assembled with MOF-based electrolytes.<sup>24</sup> It is worth noting that the maximum power density was  $17.5 \text{ mW cm}^{-2}$ , suggesting that the membrane has great potential in electrochemical device applications.<sup>6</sup> Besides, we also measured the stability of the  $\text{H}_2/\text{O}_2$  fuel cell at 80 °C and 98% RH, showing negligible degradation (Fig. S76†).

### Proton conduction mechanism

An effective proton transfer pathway is an indispensable part of proton transmission, which has an important bearing on the hydrogen bond network. Moreover, the transmission path needs to have a proton source for providing protons and a receptor for accepting protons besides sites for carrying the protons as they jump, which together facilitate proton transport. Thus, it can be perceived that our strategy of increasing the number and multiplicity of proton sources and hopping sites are especially successful and critical for the improvement of proton conduction. The specific transmission mechanisms embodying all the compounds formed by adopting this method are shown in Fig. 4. Above all, we selected a region in the **UiO-66-NH<sub>2</sub>** model structure as the proton transport path to investigate the possible mechanism (Fig. 4a). Furthermore, we compared the evolutionary process of proton transmission in the three materials using this strategy and the transmission mechanisms of two other control samples to find whether the pathway of the desired

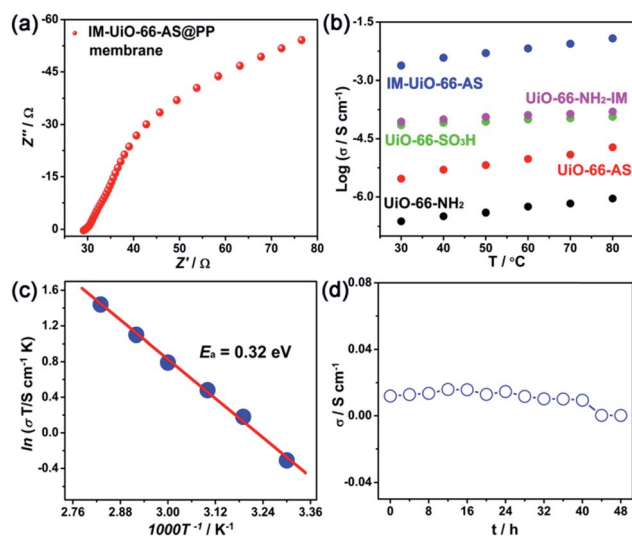


Fig. 3 (a) The Nyquist plot of IM-UiO-66-AS@PP membrane at 80 °C and under 98% RH. (b) Temperature-dependent proton conductivities of UiO-66-NH<sub>2</sub>@PP membrane (black), UiO-66-AS@PP membrane (red), UiO-66-SO<sub>3</sub>H@PP membrane (green), UiO-66-NH<sub>2</sub>-IM@PP membrane (magenta) and IM-UiO-66-AS@PP membrane (blue) (98% RH, 30–80 °C). (c) Arrhenius plot of IM-UiO-66-AS@PP membrane under 98% RH and at the temperature range of 30–80 °C. (d) Time-dependent proton conductivity of IM-UiO-66-AS@PP membrane performed at 80 °C and under 98% RH.

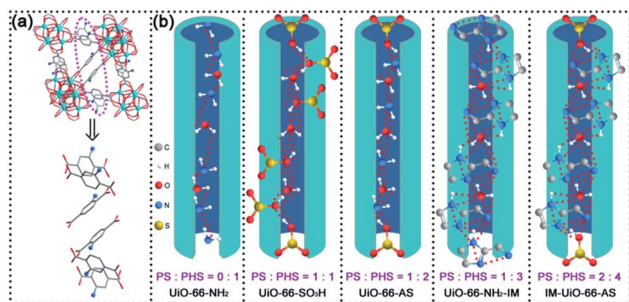


Fig. 4 (a) Possible pathway selection of the UiO-66-NH<sub>2</sub> model structure. (b) Schematic representation of the possible proton conduction mechanisms of UiO-66-NH<sub>2</sub>, UiO-66-SO<sub>3</sub>H, UiO-66-AS, UiO-66-NH<sub>2</sub>-IM and IM-UiO-66-AS. PS: proton source and PHS: proton hopping site.

product is indeed beneficial to efficient and fast proton conduction, which were consistent with our experimental results (Fig. 4b). We could intuitively see that, with the step by step modification of the material (from UiO-66-NH<sub>2</sub> to UiO-66-AS to IM-UiO-66-AS), the species of proton sources and hopping sites respectively increased from zero and one to one and two, and then to two and four. The increasing number of proton sources and hopping sites resulted in the diversification and high efficiency of the path, which undoubtedly had a vital impact on proton conduction. Specifically speaking, the transport mechanism in IM-UiO-66-AS is that the well-known hydrophilic sulfonic acid groups are prone to provide dissociated protons in the presence of water, which promotes rapid proton transfer.<sup>41</sup> On this basis, the attached imidazole group also acts as a proton source and provides hopping sites, leading to further enhancement of proton conductivity, stemming from the compound. In addition, the water molecules adsorbed under high humidity can also act as proton carriers by forming hydrogen bonds with protons released nearby. Combining Table 1 and Fig. 4b, we noted that, although UiO-66-AS has one more hopping site than UiO-66-SO<sub>3</sub>H, the number of proton sources for the latter is more than that of the former, and the number of hopping sites is the same, resulting in the slightly higher proton conductivity of UiO-66-SO<sub>3</sub>H. It is also notable that, although the proton conduction routes of UiO-66-NH<sub>2</sub>-IM are more diverse than those of IM-UiO-66-AS, as far as the proton source is concerned, the pK<sub>a</sub> value of the sulfonic acid groups is much smaller than that of the imidazole derivative, which causes lower conductivity in UiO-66-NH<sub>2</sub>-IM than that of IM-UiO-66-AS. Overall, this unique strategy of adding multiple proton sources and hopping sites endows IM-UiO-66-AS with ultrahigh proton conductivity and provides a solid and necessary grounding for the application of proton exchange membranes.

## Conclusions

In summary, we devised a hierarchical modification strategy to vary the number of proton sources and hopping sites for the improvement of proton conductivity in a stable MOF model system, in which the post-synthetic materials and membranes

finally exhibited superprotonic conductivity and outstanding long-term stability, surpassing those of the reported proton conducting MOF materials. Furthermore, the membrane was used to assemble an H<sub>2</sub>/O<sub>2</sub> fuel cell, and the maximum power density was 17.5 mW cm<sup>-2</sup>. Most importantly, we believe that this strategy can be used further for the development of more stable and high-performance MOF-based proton conductors. Moreover, such strategic hierarchical improvisation of proton conductivity in MOFs can provide an in-depth understanding of the mechanisms for the development of next-generation PEMs and solid electrolytes.

## Conflicts of interest

There are no conflicts to declare.

## Acknowledgements

This work was financially supported by NSFC (No. 21622104, 21701085, 21871141, 21871142 and 21901122); the NSF of Jiangsu Province of China (No. BK20171032); the Natural Science Research of Jiangsu Higher Education Institutions of China (No. 17KJB150025 and 19KJB150011) and Project funded by China Postdoctoral Science Foundation (No. 2018M630572 and 2019M651873); Priority Academic Program Development of Jiangsu Higher Education Institutions and the Foundation of Jiangsu Collaborative Innovation Center of Biomedical Functional Materials.

## Notes and references

- Y. Ye, W. Guo, L. Wang, Z. Li, Z. Song, J. Chen, Z. Zhang, S. Xiang and B. Chen, *J. Am. Chem. Soc.*, 2017, **139**, 15604–15607.
- Y. Guo, Z. Jiang, W. Ying, L. Chen, Y. Liu, X. Wang, Z.-J. Jiang, B. Chen and X. Peng, *Adv. Mater.*, 2018, **30**, 1705155.
- W. J. Phang, W. R. Lee, K. Yoo, D. W. Ryu, B. Kim and C. S. Hong, *Angew. Chem., Int. Ed.*, 2014, **53**, 8383–8387.
- G. K. H. Shimizu, J. M. Taylor and S. Kim, *Science*, 2013, **341**, 354.
- D. Umeyama, S. Horike, M. Inukai and S. Kitagawa, *J. Am. Chem. Soc.*, 2013, **135**, 11345–11350.
- J. Zhang, H.-J. Bai, Q. Ren, H.-B. Luo, X.-M. Ren, Z.-F. Tian and S. Lu, *ACS Appl. Mater. Interfaces*, 2018, **10**, 28656–28663.
- X.-Y. Dong, J.-H. Wang, S.-S. Liu, Z. Han, Q.-J. Tang, F.-F. Li and S.-Q. Zang, *ACS Appl. Mater. Interfaces*, 2018, **10**, 38209–38216.
- X.-Y. Dong, J.-J. Li, Z. Han, P.-G. Duan, L.-K. Li and S.-Q. Zang, *J. Mater. Chem. A*, 2017, **5**, 3464–3474.
- A. Shigematsu, T. Yamada and H. Kitagawa, *J. Am. Chem. Soc.*, 2011, **133**, 2034–2036.
- Y. Wang, Z. Tao, X. Yin, J. Shu, L. Chen, D. Sheng, Z. Chai, T. E. Albrecht-Schmitt and S. Wang, *Inorg. Chem.*, 2015, **54**, 10023–10029.
- B. Liu, D. Cheng, H. Zhu, J. Du, K. Li, H.-Y. Zang, H. Tan, Y. Wang, W. Xing and Y. Li, *Chem. Sci.*, 2019, **10**, 556–563.

- 12 D.-W. Lim, M. Sadakiyo and H. Kitagawa, *Chem. Sci.*, 2019, **10**, 16–33.
- 13 D. Umeyama, S. Horike, M. Inukai, T. Itakura and S. Kitagawa, *J. Am. Chem. Soc.*, 2012, **134**, 12780–12785.
- 14 T. Yamada, K. Otsubo, R. Makiura and H. Kitagawa, *Chem. Soc. Rev.*, 2013, **42**, 6655–6669.
- 15 Q. Tang, Y. Liu, S. Liu, D. He, J. Miao, X. Wang, G. Yang, Z. Shi and Z. Zheng, *J. Am. Chem. Soc.*, 2014, **136**, 12444–12449.
- 16 M. Sadakiyo, T. Yamada and H. Kitagawa, *J. Am. Chem. Soc.*, 2009, **131**, 9906–9907.
- 17 S. Khatua, A. K. Bar, J. A. Sheikh, A. Clearfield and S. Konar, *Chem.–Eur. J.*, 2018, **24**, 872–880.
- 18 X. Li, X. Sun, X. Li, Z. Fu, Y. Su and G. Xu, *Cryst. Growth Des.*, 2015, **15**, 4543–4548.
- 19 S. Pili, P. Rought, D. I. Kolokolov, L. Lin, I. da Silva, Y. Cheng, C. Marsh, I. P. Silverwood, V. García Sakai, M. Li, J. J. Titman, L. Knight, L. L. Daemen, A. J. Ramirez-Cuesta, C. C. Tang, A. G. Stepanov, S. Yang and M. Schröder, *Chem. Mater.*, 2018, **30**, 7593–7602.
- 20 K. Zhang, X. Xie, H. Li, J. Gao, L. Nie, Y. Pan, J. Xie, D. Tian, W. Liu, Q. Fan, H. Su, L. Huang and W. Huang, *Adv. Mater.*, 2017, **29**, 1701804.
- 21 F.-M. Zhang, L.-Z. Dong, J.-S. Qin, W. Guan, J. Liu, S.-L. Li, M. Lu, Y.-Q. Lan, Z.-M. Su and H.-C. Zhou, *J. Am. Chem. Soc.*, 2017, **139**, 6183–6189.
- 22 B. Joarder, J.-B. Lin, Z. Romero and G. K. H. Shimizu, *J. Am. Chem. Soc.*, 2017, **139**, 7176–7179.
- 23 S. S. Park, A. J. Rieth, C. H. Hendon and M. Dincă, *J. Am. Chem. Soc.*, 2018, **140**, 2016–2019.
- 24 Y.-S. Wei, X.-P. Hu, Z. Han, X.-Y. Dong, S.-Q. Zang and T. C. W. Mak, *J. Am. Chem. Soc.*, 2017, **139**, 3505–3512.
- 25 J. M. Taylor, K. W. Dawson and G. K. H. Shimizu, *J. Am. Chem. Soc.*, 2013, **135**, 1193–1196.
- 26 S.-L. Li and Q. Xu, *Energy Environ. Sci.*, 2013, **6**, 1656–1683.
- 27 S. Horike, D. Umeyama, M. Inukai, T. Itakura and S. Kitagawa, *J. Am. Chem. Soc.*, 2012, **134**, 7612–7615.
- 28 H. Furukawa, K. E. Cordova, M. O’Keeffe and O. M. Yaghi, *Science*, 2013, **341**, 1230444.
- 29 T. He, Y.-Z. Zhang, H. Wu, X.-J. Kong, X.-M. Liu, L.-H. Xie, Y. Dou and J.-R. Li, *ChemPhysChem*, 2017, **18**, 3245–3252.
- 30 M. Inukai, S. Horike, W. Chen, D. Umeyama, T. Itakura and S. Kitagawa, *J. Mater. Chem. A*, 2014, **2**, 10404–10409.
- 31 K. Müller, J. Helfferich, F. Zhao, R. Verma, A. B. Kanj, V. Meded, D. Bléger, W. Wenzel and L. Heinke, *Adv. Mater.*, 2018, **30**, 1706551.
- 32 P. G. M. Mileo, K. Adil, L. Davis, A. Cadiau, Y. Belmabkhout, H. Aggarwal, G. Maurin, M. Eddaoudi and S. Devautour-Vinot, *J. Am. Chem. Soc.*, 2018, **140**, 13156–13160.
- 33 S. S. Nagarkar, S. M. Unni, A. Sharma, S. Kurungot and S. K. Ghosh, *Angew. Chem., Int. Ed.*, 2014, **53**, 2638–2642.
- 34 N. E. Wong, P. Ramaswamy, A. S. Lee, B. S. Gelfand, K. J. Bladek, J. M. Taylor, D. M. Spasyuk and G. K. H. Shimizu, *J. Am. Chem. Soc.*, 2017, **139**, 14676–14683.
- 35 S. Kim, B. Joarder, J. A. Hurd, J. Zhang, K. W. Dawson, B. S. Gelfand, N. E. Wong and G. K. H. Shimizu, *J. Am. Chem. Soc.*, 2018, **140**, 1077–1082.
- 36 N. C. Burtch, H. Jasuja and K. S. Walton, *Chem. Rev.*, 2014, **114**, 10575–10612.
- 37 A. J. Howarth, Y. Liu, P. Li, Z. Li, T. C. Wang, J. T. Hupp and O. K. Farha, *Nat. Rev. Mater.*, 2016, **1**, 15018.
- 38 J. H. Cavka, S. Jakobsen, U. Olsbye, N. Guillou, C. Lamberti, S. Bordiga and K. P. Lillerud, *J. Am. Chem. Soc.*, 2008, **130**, 13850–13851.
- 39 F. Yang, H. Huang, X. Wang, F. Li, Y. Gong, C. Zhong and J.-R. Li, *Cryst. Growth Des.*, 2015, **15**, 5827–5833.
- 40 F. Yang, G. Xu, Y. Dou, B. Wang, H. Zhang, H. Wu, W. Zhou, J.-R. Li and B. Chen, *Nat. Energy*, 2017, **2**, 877–883.
- 41 W. J. Phang, H. Jo, W. R. Lee, J. H. Song, K. Yoo, B. Kim and C. S. Hong, *Angew. Chem., Int. Ed.*, 2015, **54**, 5142–5146.
- 42 S.-Y. Zhu and B. Yan, *Dalton Trans.*, 2018, **47**, 11586–11592.
- 43 V. G. Ponomareva, K. A. Kovalenko, A. P. Chupakhin, D. N. Dybtsev, E. S. Shutova and V. P. Fedin, *J. Am. Chem. Soc.*, 2012, **134**, 15640–15643.
- 44 M. Kandiah, S. Usseglio, S. Svelle, U. Olsbye, K. P. Lillerud and M. Tilset, *J. Mater. Chem.*, 2010, **20**, 9848–9851.
- 45 S.-Y. Zhu and B. Yan, *Dalton Trans.*, 2018, **47**, 11586–11592.
- 46 Z. Liang, W. Chen, J. Liu, S. Wang, Z. Zhou, W. Li, G. Sun and Q. Xin, *J. Membr. Sci.*, 2004, **233**, 39–44.
- 47 R. Kardanpour, S. Tangestaninejad, V. Mirkhani, M. Moghadam, I. Mohammadpoor-Baltork and F. Zadehahmadi, *J. Solid State Chem.*, 2015, **226**, 262–272.
- 48 Z. Sun, G. Li, H.-o. Liu and L. Liu, *Appl. Catal., A*, 2013, **466**, 98–104.
- 49 S. Wang, M. Wahiduzzaman, L. Davis, A. Tissot, W. Shepard, J. Marrot, C. Martineau-Corcus, D. Hamdane, G. Maurin, S. Devautour-Vinot and C. Serre, *Nat. Commun.*, 2018, **9**, 4937.
- 50 P. Ramaswamy, N. E. Wong, B. S. Gelfand and G. K. H. Shimizu, *J. Am. Chem. Soc.*, 2015, **137**, 7640–7643.
- 51 X.-M. Li, L.-Z. Dong, S.-L. Li, G. Xu, J. Liu, F.-M. Zhang, L.-S. Lu and Y.-Q. Lan, *ACS Energy Lett.*, 2017, **2**, 2313–2318.